

Multiphysics Model of Continuous Casting of Steel Beam-Blanks

Brian G. Thomas¹, Seid Koric², Lance C. Hibbeler¹, Rui Liu¹

¹ University of Illinois at Urbana-Champaign, Department of Mechanical Science and Engineering, 1206 West Green Street, Urbana, IL USA 61801. Phone: 217-333-6919. E-mail: bgthomas@uiuc.edu

² National Center for Supercomputing Applications, University of Illinois at Urbana-Champaign, 1205 W. Clark St, Urbana, IL USA 61801. Phone: 217-265-8410. E-mail: skoric@ncsa.uiuc.edu

Abstract

Separate three-dimensional models of thermo-mechanical behavior of the solidifying shell, turbulent fluid flow in the liquid pool, and thermal distortion of the mold are combined to create an accurate multiphysics model of metal solidification at the continuum level. The new system is applied to simulate continuous casting of steel in a commercial beam-blank caster with complex geometry. A transient coupled elastic-viscoplastic model computes temperature and stress in a transverse slice through the mushy and solid regions of the solidifying metal. This Lagrangian model features an efficient numerical procedure to integrate the constitutive equations of the delta-ferrite and austenite phases of solidifying steel shell using a fixed-grid finite-element approach. The Navier-Stokes equations are solved in the liquid pool using the standard K- ϵ turbulent flow model with standard wall laws at the mushy zone edges that define the domain boundaries. The superheat delivered to the shell is incorporated into the thermal-mechanical model of the shell using a new enhanced latent heat method. Temperature and thermal distortion modeling of the complete complex-shaped mold includes the tapered copper plates, water cooling slots, backing plates, and nonlinear contact between the different components. Heat transfer across the interfacial gaps between the shell and the mold is fully coupled with the stress model to include the effect of shell shrinkage and gap formation on lowering the heat flux. The model is validated by comparison with analytical solutions of benchmark problems of conduction with phase change, and thermal stress in an unconstrained solidifying plate. Finally, results from the complete system are shown to compare favorably with plant measurements of shell thickness.

Key Words

Solidification, Multiphysics, Thermal-Stress, Fluid Flow, Superheat, Viscoplastic, Turbulence, Continuous Casting

Introduction

Many manufacturing processes, such as continuous casting of steel, involve multiple coupled phenomena, including fluid flow, heat transfer, solidification, distortion, and stress generation. As the demand for better computer simulations of solidification processes increases, there is a growing need to include the effects of fluid flow into thermo-mechanical analyses of commercial processes.

Some previous coupled models of these phenomena solve all of the equations simultaneously in the same computational domain, and have been restricted by computing power [1, 2]. Lee and coworkers [3] showcased multiphysics modeling by coupling a 3-D finite-difference model of fluid flow with a 2-D transient thermal-stress model to predict solidification, gap formation, stress, and crack formation in a beam-blank caster. Teskeredzic et al. [4] used a 2D multiphysics finite-volume method for simultaneous prediction of physical phenomena during a solid/liquid

phase change. Neither prediction was validated with plant measurements. Some researchers attempted to decouple the thermal-fluid simulation from the stress analysis [5-10] but this neglects the important effects of shrinkage and deformation on heat transfer, such as that caused by increased pressure or gap formation between the casting and the mold [11].

In many processes, such as steel continuous casting, the fluid flow simulation can be reasonably decoupled from the thermal-stress analysis because the liquid pool shape can be estimated a-priori. Then, the mechanical influence of fluid on the solid shell can be modeled with hydrostatic pressure boundary conditions [12]. A separate simulation of fluid flow in a domain containing only the liquid cavity can readily output the "superheat flux" that delivers heat across the domain boundary that represents the solidification front, such as characterized by the liquidus temperature. Recently Koric et al. [13, 14] have shown how "superheat flux" can be incorporated into a transient simulation of heat transfer phenomena in the mushy and solid regions by enhancing the latent

heat in the mushy zone without an explicit need to track the solidification front. The procedure has been added into the commercial package ABAQUS [15] with a user-defined subroutine UMATHT. This model system satisfies the governing equations for conservation of mass, momentum, and energy in the molten steel, the solidifying shell, and the solid mold using three different models and three different computational domains. In the present work, this approach is applied to perform a realistic simulation of turbulent fluid flow, heat transfer, solidification, stress, and mold distortion of a commercial beam-blank continuous-casting mold, shown in **Figure 1**.

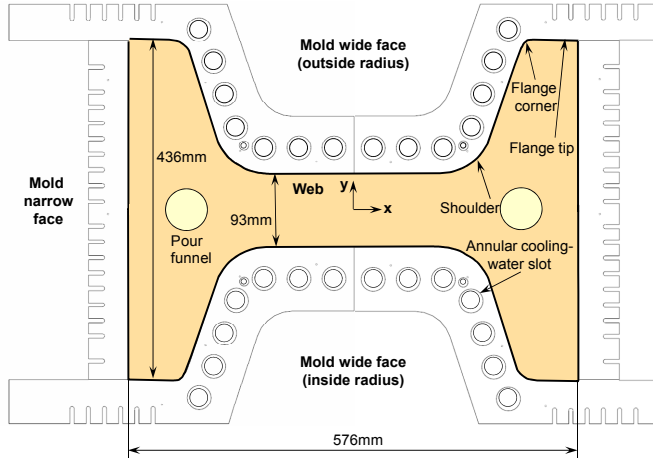


Figure 1: Schematic of beam blank caster (top view)

Solidifying Shell Model

The solidifying steel shell is modeled as a transverse Lagrangian slice that moves down through the mold at the casting speed. Several previous thermal-mechanical models of continuous casting have used this approach [12-14,16-27]. Because the domain and material velocities are identical, the Lagrangian formulation removes the advection terms from the governing equations. This is a slight over-simplification because the mushy zone does not move at exactly the casting speed. The constitutive equations are defined in rate form:

$$\dot{\sigma} = \mathbb{C} : (\dot{\epsilon} - \dot{\epsilon}^{th} - \dot{\epsilon}^{ie}) \quad (1)$$

where \mathbb{C} is the fourth-order tensor of elastic constants assumed here to be isotropic, $\dot{\epsilon}^{th}$ is the thermal strain rate tensor calculated from temperatures resulting from the solution of the transient heat-conduction equation with solidification, $\dot{\epsilon}^{ie}$ is the inelastic strain rate tensor, and $\dot{\epsilon}$ is the total linearized strain rate tensor, calculated from:

$$\dot{\epsilon} = \frac{d}{dt} \left[\frac{1}{2} (\nabla \mathbf{u} + (\nabla \mathbf{u})^T) \right] \quad (2)$$

where \mathbf{u} is the displacement vector. Note that this formulation does not include the effect of the temperature dependence of the elastic constants on the stress rate. This small-strain mechanical model is reasonable for casting processes.

Temperature and phase-dependent enthalpy, thermal conductivity, thermal expansion, and elastic modulus [26] were calculated for 0.071 % wt. C plain carbon steel. The volume fractions of the liquid, delta, and austenite phases are calculated according to a multicomponent microsegregation model [27]. Other simulation conditions are listed in Table 1.

Strand section size (mold top)	576 x 436 x 93 mm
Working mold length	660.4 mm
Total taper at flange	2.33 mm
Total taper at shoulder edge	-2.22 mm
Total taper at wide face	0.48 mm
Total taper at narrow face	3.0 mm
Mold contact resistance heat transfer coefficient, h_{mold}	2500 W/m ² /K
Casting speed	0.889 m/min
Mold thermal conductivity	370 W/m·K
Steel grade	0.071 % wt. C
Initial temperature (strand)	1523.70 °C
Initial temperature (mold)	285 °C
Liquidus temperature	1518.70 °C
Solidus temperature	1471.95 °C
Cooling water temperature	34.5 °C

Table 1: Simulation Conditions

The inelastic strain includes both strain-rate independent plasticity and time-dependent creep. Creep is significant at the high temperatures of the solidification processes and is indistinguishable from plastic strain. The following unified constitutive equation [28] defines inelastic strain in the solid austenite phase:

$$\dot{\bar{\epsilon}}_{ie} [\text{sec}^{-1}] = f_c (\bar{\sigma} [\text{MPa}] - f_1 \bar{\epsilon}_{ie} |\bar{\epsilon}_{ie}|^{f_2-1})^{f_3} \exp\left(-\frac{Q}{T[K]}\right) \quad (3)$$

where Q is an activation energy, $\bar{\sigma}$ is effective (Von-Mises) stress, $\bar{\epsilon}_{ie}$ is effective inelastic strain, T is temperature, and the empirical temperature- and composition-dependant constants are defined elsewhere [20,21,23]. The modified power-law model developed by Zhu [20] is used to simulate the delta-ferrite phase, which exhibits significantly higher creep rates and lower strength than the austenite phase. The delta-ferrite constitutive model is used whenever the volume fraction of ferrite is greater than 10%. To enforce negligible liquid strength in mushy and liquid zones before solidification takes place, an isotropic elastic-perfectly-plastic rate-independent constitutive model is used when the temperature is above the solidus temperature. The yield stress is chosen small

The governing equations are incrementally solved using the finite-element method [29] in ABAQUS [15] using a fully implicit stepwise-coupled algorithm for the time integration of the governing equations [20,21]. The highly-nonlinear elastic-viscoplastic constitutive laws are integrated by solving a system of two ordinary differential equations defined at each local material point using the backward-Euler method with a bounded Newton-Raphson method [13] in the user subroutine UMAT [15]. In each time step the thermal problem is first solved, and then the resulting thermal strains are used to drive the mechanical problem. Global Newton-Raphson iterations continue until tolerances for both equation systems are satisfied before proceeding to the next time step.

The diagram illustrates a cross-section of a continuous casting mold. The mold is shown as a U-shaped container. Inside, the strand is depicted with a blue outer shell and a white inner liquid core. Key regions and features are labeled:

- Left Flange Corner**: The top-left corner of the mold.
- Right Flange Corner**: The top-right corner of the mold.
- Middle Flange**: The top horizontal section of the mold.
- Interfacial Gap: Thermo-Mechanical Contact**: The gap between the mold wall and the strand shell.
- Mold Surface: Prescribe: Temperature, Taper, and Mold Distortion**: The inner surface of the mold.
- Mold**: The container itself.
- Strand (shell & liquid)**: The material being cast.
- Superheat (liquid)**: The liquid core of the strand.
- End Shoulder**: The shoulder of the strand near the mold exit.
- Mid WF**: Mid Width Flange.
- Mid. Shoulder**: Mid Shoulder.
- Mid NF**: Mid Neck Flange.

This 2-D transient model also comprises a 3-D solution at steady state. The slice begins at the top of the liquid steel pool, where the uniform initial conditions are the pouring temperature, zero displacement, zero strain, and zero stress. The 2-D assumption is valid for the thermal analysis, owing to

Fluid Flow Model

Buoyancy forces are negligible relative to the flow inertia, as indicated by $Gr/Re^2 \sim 10^{-2}-10^{-4}$, where Gr is the Grashoff number and Re is the Reynolds number. The velocity and temperature fields are thus decoupled, as the flow affects the temperature but the temperature does not affect the flow.

The shape of the domain is specified by extracting the position of the solidification front (liquidus temperature) from the solidifying shell model, and the symmetry planes of the mold. Fluid enters the liquid pool through a funnel that catches the gravity-driven stream from the tundish bottom. This is modeled with fixed $v=1.854\text{m/s}$, $K=0.464\text{m}^2/\text{s}^2$, and $\varepsilon=2.077\text{m}^2/\text{s}^3$ on the 25.5mm diameter inlet boundary plane on the top surface that represents the pouring funnel outlet.

Figure 3 shows the velocity and temperature distributions on the center planes and top plane (10-

mm below the liquid surface) calculated with the 3D fluid flow – heat transfer simulation of 606,720 hexahedral cells.

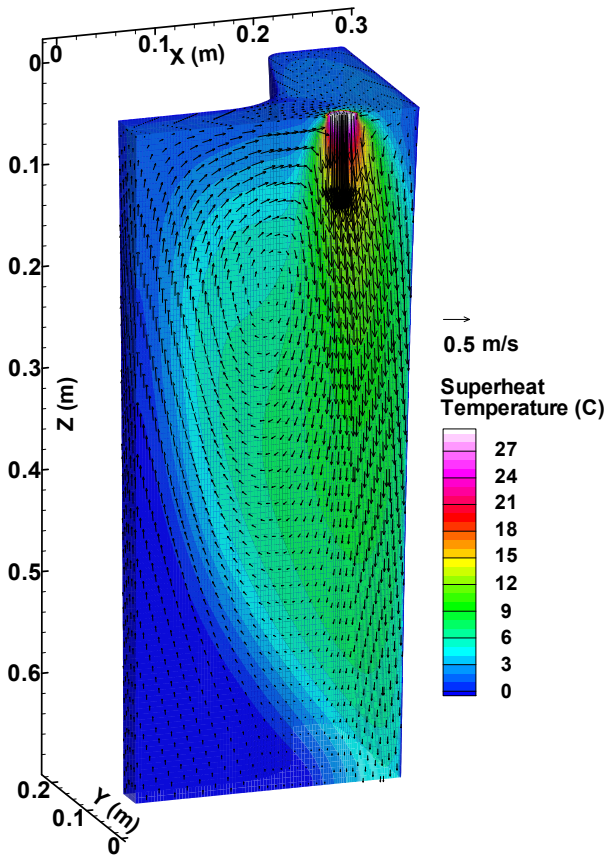


Figure 3: Velocity and Temperature Distributions in the Liquid Pool

Mold Model

In addition to supporting the shell to determine its shape, the copper mold in the continuous casting process extracts heat from the molten steel by means of cooling water flowing through circular channels and rectangular slots. The mold assembly consists of two wide faces, two narrow faces, and their respective water boxes. The steel water boxes serve to circulate the water in the mold and also increase the rigidity of the assembly to reduce the effect of the thermal distortion of the mold when it heats up to operating temperatures. In this work, a three-dimensional finite-element model of one symmetric fourth of the mold assembly was constructed to capture the effects of mold distortion and variable mold surface temperature on the solidifying steel shell. The model mold and water box geometries include the curvature and applied taper of the hot faces, water channels, and bolt holes. The taper is applied to the mold pieces to accommodate the solidification shrinkage of the solid steel.

The mesh consisted of 263,879 nodes and 1,077,166 tetrahedron, wedge, and hexahedron elements. The standard equilibrium equations, small-strain-

displacement equations, and linear-elastic constitutive equations for thermal stress analysis were solved in this model using ABAQUS [15]. The effect of creep in the copper was neglected owing to its small effect on mold distortion [36]. Appropriate partial contact between the two mold pieces and two backing plates was enforced manually by iteratively applying constraint equations on contacting nodes. The mold bolts and tie rods were simulated using linear truss elements and were appropriately pre-stressed. The heat flux applied to the hot faces of the mold was extracted from the shell-mold surface in the shell model.

The calculated temperature and distortion results are presented in **Figure 4**. In addition to providing insight into thermo-mechanical behavior of the mold, this model provides temperature and displacement boundary conditions to the shell model. More detail of this model can be found elsewhere [26].

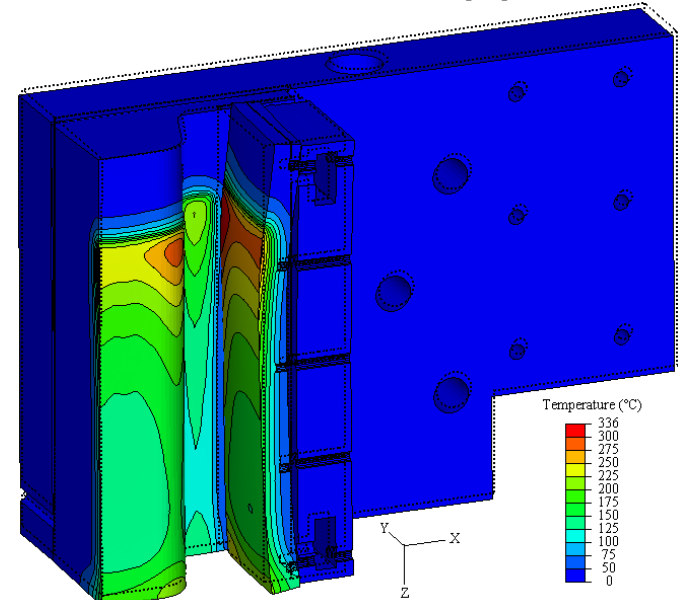


Figure 4: Temperature and distorted shape of mold (20x magnified distortion)

Fluid / Shell Interface Treatment

Results from the fluid flow model of the liquid domain affect the solidifying shell model by the heat flux crossing the boundary, which represents the solidification front, or liquidus temperature. This “superheat flux” q_{super} can be incorporated into a fixed-grid simulation of heat transfer phenomena in the mushy and solid regions by enhancing the latent heat [14] used in the shell model. This new method enables accurate uncoupling of complex heat-transfer phenomena into separate simulations of the fluid flow region and the mushy-solid region [14]. Starting with the Stefan interface condition [30], the additional latent heat ΔH_f to account for superheat flux delivered from the liquid pool is calculated from:

$$\Delta H_f = \frac{q_{super}(\mathbf{x}, t)}{\rho_{solid} |v_{interface}|} \quad (4)$$

where ρ_{solid} is the solid density, \mathbf{x} is distance around the perimeter, and t is time below the meniscus. The latent heat enhancement is added to the original latent heat and enthalpy in the transient heat conduction equation via a UMATHT user subroutine in ABAQUS [15]. In the transient shell model, the interface speed $v_{interface}$ can be estimated from the local cooling rate \dot{T} and temperature gradient $\|\nabla T\|$ at every time and material point near the solidification front.

$$v_{interface} = \frac{\dot{T}}{\|\nabla T\|} = \frac{\Delta T}{\Delta t} \frac{1}{\|\nabla T\|} \quad (5)$$

This method sometimes produces excessive and fluctuating latent heat values when temperature increments ΔT are driven to be very small by the global Newton-Raphson iterative solution procedures, particularly at early simulation times and when superheat flux is high. When the maximum latent heat enhancement reaches 40 times the initial value of the latent heat, the $v_{interface}$ estimate switches to an analytical solution based on the classical 1-D solidified-metal-shell control solidification solution [30] with the addition of superheat:

$$c_{ps}(T_{liq} - T_{surf}) = \phi \exp(\phi^2) \operatorname{erf}(\phi) \sqrt{\pi} \left(H_f + \frac{q_{super}(\mathbf{x}, t)}{\rho \sqrt{\alpha_s} \phi \frac{1}{\sqrt{t}}} \right) \quad (6)$$

The above equation is solved for ϕ for every time increment and velocity is calculated as:

$$v_{interface}(t) = \phi \sqrt{\alpha_s / t} \quad (7)$$

This method gives an accurate and smooth estimate of the interface velocity, and was shown to perform well in both one- and two-dimensional solidification problems [14].

The superheat flux $q_{super}(\mathbf{p}, z)$ that is calculated at the boundaries of the 3-D Eulerian fluid-flow model must be converted to a function of space and time for the Lagrangian shell model $q_{super}(\mathbf{x}, t)$. The perimeter coordinate $\mathbf{p}(x, y)$ around the surface of the flow model is chosen to be the liquidus isotherm. The surface coordinates and the superheat data are stored in arrays of $N_{perimeter}$ points around the perimeter for each of the N_z layers of nodes below the meniscus. At each given time and material point in the shell model within the mushy zone, the axial coordinate is found simply from $z = v_c \cdot t$. The array coordinates are searched to find the indices i and

$i+1$ ($1 \leq i \leq N_{perimeter}$) and j and $j+1$ ($1 \leq j \leq N_z$) which bound the material point in the Lagrangian shell model. The corresponding superheat fluxes $q_{super}(i, j)$, $q_{super}(i+1, j)$, $q_{super}(i, j+1)$, and $q_{super}(i+1, j+1)$ are then bilinearly interpolated using standard interpolation functions for a 4-node quadrilateral finite element, [29], with element-based coordinates $\xi = 2(p - p_i)/(p_{i+1} - p_i) - 1$ in the perimeter direction and $\eta = 2(z - z_j)/(z_{j+1} - z_j) - 1$ in the axial direction, where p here is taken as x on the wideface and y on the narrow face.

Figure 5 shows a 3-D view of the superheat flux distribution on the shell interface calculated from the CFD turbulent flow model. The fluid flow causes uneven distribution of superheat fluxes that are greatest midway down the inner shoulder, and least in the flange and center of the wide face. These variations in turn cause local shell thinning and temperature changes, which affect the thermal stress behaviour.

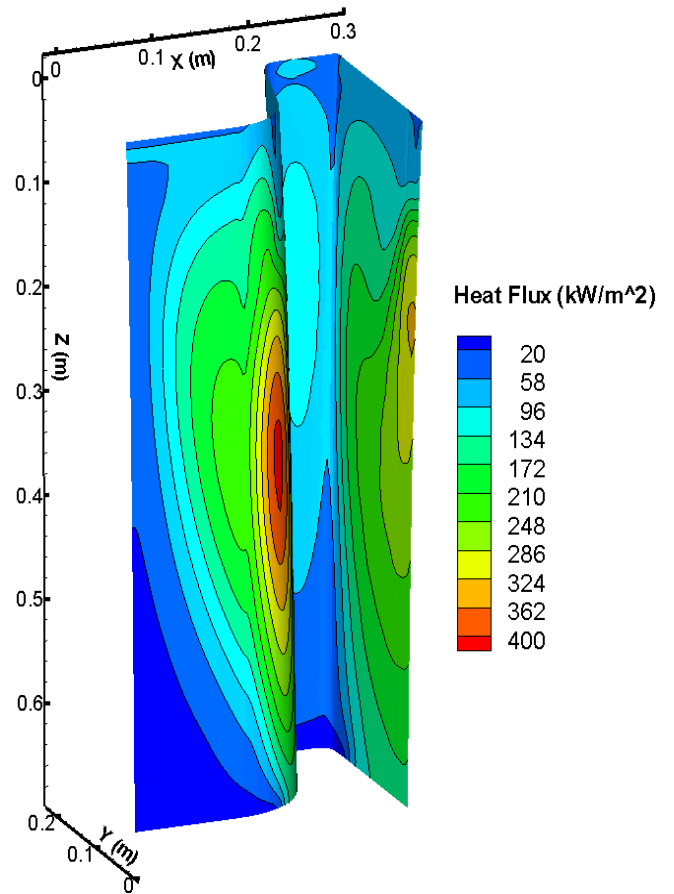


Figure 5: 3D view of the superheat flux distribution on the shell interface

The effect of the ferrostatic pressure in the liquid pool is treated in the shell model as a linearly-increasing distributed load that pushes the solidifying steel shell towards the mold. This condition was treated using the ABAQUS user subroutine DLOAD [15].

Shell/Mold Interface Treatment

Two-way thermo-mechanical coupling between the shell and mold is needed because the stress analysis depends on temperature via thermal strains and material properties, and the heat conducted between the mold and steel strand depends strongly on distance between the separated surfaces calculated from the mechanical solution. Heat transfer across the interfacial gap between the shell and the mold wall surfaces is defined with a resistor model that depends on the thickness of gap calculated by the stress model. The total heat transfer q_{gap} occurs along two parallel paths, due to radiation, h_{rad} , and conduction, h_{cond} , as follows:

$$q_{gap} = -k \partial T / \partial n = -(h_{rad} + h_{cond})(T_{shell} - T_{mold}) \quad (8)$$

where n is in the direction normal to the surface. The radiation heat transfer coefficient is calculated across the transparent liquid portion of the mold slag layer:

$$h_{rad} = \frac{\sigma_{SB}}{\frac{1}{\epsilon_{shell}} + \frac{1}{\epsilon_{mold}} - 1} (T_{shell} + T_{mold})(T_{shell}^2 + T_{mold}^2) \quad (9)$$

where $\sigma_{SB} = 5.6704 \cdot 10^{-8} \text{ W m}^{-2} \text{ K}^{-4}$ is the Stefan-Boltzmann constant, $\epsilon_{shell} = \epsilon_{mold} = 0.8$ are the emissivities of the shell and mold surface, and T_{shell} and T_{mold} are their current temperatures, respectively. The conduction heat transfer coefficient depends on four resistances connected in series:

$$\frac{1}{h_{cond}} = \frac{1}{h_{mold}} + \frac{(d_{gap} - d_{slag})}{k_{air}} + \frac{d_{slag}}{k_{slag}} + \frac{1}{h_{shell}} \quad (10)$$

The first resistance, $1/h_{mold}$, is the contact resistance between mold wall surface and the solidified mold slag film. The contact heat transfer coefficient h_{mold} is chosen to be 2500 W/m^2 [24]. The second resistance is associated with conduction across the air gap assuming $k_{air} = 0.06 \text{ W/m} \cdot \text{K}$. The thickness of the air gap is determined from the results of the mechanical contact analysis. An artificial constant slag film thickness, $d_{slag} = 0.1 \text{ mm}$, is adopted in this work to prevent non-physical behavior associated with very small gaps [24]. The third resistance is due to conduction through the slag film assuming $k_{slag} = 1.0 \text{ W/m} \cdot \text{K}$. The final term is the contact resistance between the slag film and the strand, where the shell contact heat transfer coefficient h_{shell} depends greatly on temperature. This shell-slag contact heat-transfer coefficient decreases greatly as the shell surface temperature drops below the solidification temperature of the mold slag [25]. These equations

were implemented via the user-defined subroutine GAPCON into ABAQUS [15].

The size of the gap is determined through the “softened” exponential contact algorithm built into ABAQUS/Standard [15], knowing the position of the mold wall and shell surfaces \mathbf{x}_{mold} and \mathbf{x}_{shell} :

$$d_{gap}(\mathbf{x}, t) = \|\mathbf{x}_{shell}(t) - \mathbf{x}_{mold}(\mathbf{x}, t)\| \quad (11)$$

The first iteration of the shell model used the nominal (undistorted) shape of the mold. For the second iteration of the shell model, the results on the hotface boundary of the 3-D Eulerian mold distortion model were post-processed to create a database of surface temperature, $T_{mold}(\mathbf{p}, z)$, and surface position, $\mathbf{x}_{mold}(\mathbf{p}, z)$, for points on the transverse perimeter of the hot face \mathbf{p} and distance down the mold, z . The same process used to interpolate the superheat flux data described in Section 6 was used to interpolate the T_{mold} and \mathbf{x}_{mold} data into $T_{mold}(\mathbf{x}, t)$ and $\mathbf{x}_{mold}(\mathbf{x}, t)$ on the mold surfaces for Eqs. 8 and 9 of the shell model as a function of time below the meniscus, $t = z/v_c$. A time-varying displacement was applied to each point on the hot face to re-create the distorted shape of the mold that the Lagrangian shell domain encounters as it moves through the mold, using the ABAQUS user subroutine DISP [15].

Validation of the Numerical Models

The thermo-mechanical solidification model used in this work was validated by comparison with the classic semi-analytical solution of thermal stresses in an unconstrained solidifying plate [37]. A one-dimensional model of this test casting can produce the complete 3-D stress and strain state if the condition of generalized plane strain is imposed in both the width (y) and length (z) directions [21]. The domain adopted for this problem model was with the strand in a Lagrangian frame of reference like the full beam-blank model. The domain consists of a thin slice through the plate thickness using 2-D 4-node generalized plane strain elements (in the axial z direction) implemented in ABAQUS. The second generalized plane strain condition was imposed in the y -direction (parallel to the surface) by coupling the displacements of all nodes along the bottom edge of the slice domain. A fixed temperature was imposed at the left boundary, with other boundaries insulated.

The material in this problem has elastic-perfectly plastic constitutive behavior. The yield stress drops linearly with temperature from 20 MPa at 1000 °C to zero at the solidus temperature 1494.4 °C, which was approximated by 0.03 MPa at the solidus temperature. A very narrow mushy region, 0.1 °C, is used to approximate the single melting temperature assumed in the analytical solution. The temperature and stress distributions across the solidifying shell of

the numerical method match closely with the analytical solution. More details about this model validation can be found elsewhere [13] including comparisons with other less-efficient integration methods and a convergence study. The method for modeling superheat by enhancing latent heat [14] was also tested on the same slice domain and compared with a 1D analytical solution for conduction with phase change [30]. The superheat flux is best calculated with simultaneous modeling of fluid flow. Instead initial temperature is raised by 50 °C, thus providing a superheat flux driven by the temperature difference between T_{init} and T_{liq} , assuming stagnant liquid. Since the entire problem including the liquid pool starting from the initial temperature of T_{init} can be solved for this simplified test using the conventional solution method built into ABAQUS, the heat flux is extracted from that simulation as a function of time at the moving interface front (i.e. for the points that are at temperature T_{liq}). It represents the superheat flux entering the narrow mushy zone from the liquid pool. Next, the problem was rerun using the enhanced latent heat method in Abaqus with UMATHT. Here, the initial temperature is just above T_{liq} , thus providing no superheat through the temperature difference between T_{init} and T_{liq} . Instead, the latent heat enhancement needed in Eq. (5) was calculated from the superheat flux. A comparison of shell thickness (defined by T_{ref}) between the enhanced latent heat method, and the analytical solution is shown in **Figure 6**, both with and without superheat. Naturally, solidification is faster with no superheat. The new enhanced latent heat method is demonstrated to accurately account for superheat in transient solidification problems.

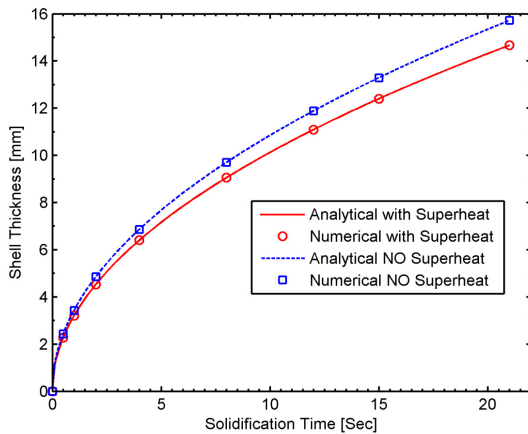


Figure 6: Shell Thickness History Comparison

Multiphysics Model of Beam Blank

The entire multiphysics model was applied to solve for fluid-flow, temperature, stress, and deformation in a complex-shaped beam blank caster under realistic continuous casting conditions. **Figure 7** is a flow

chart of the solution strategy for the thermo-mechanical-fluid flow model of steel continuous casting. First, the thermo-mechanical model of the solidifying shell is run assuming a uniform superheat distribution driven by the temperature difference between T_{init} and T_{liq} , and artificially increasing thermal conductivity in the liquid region by 7-fold. The heat fluxes leaving the shell surface provide the boundary conditions for the thermo-mechanical model of the mold, which in turns supplies the next run of the shell model with mold temperature and thermal distortion boundary conditions. The position of the solidification front in the shell model defines an approximate shape of the liquid pool for the fluid flow model, which is used to calculate the superheat flux distribution. Finally, an improved thermo-mechanical model of solidifying shell is re-run which includes the effects of the superheat distribution and mold distortion, and completes the first iteration of the multiphysics model. Because the shell profile from the improved thermo-mechanical model has little effect on superheat results in the liquid pool, a single multiphysics iteration is sufficient to produce an accurate shell growth prediction.

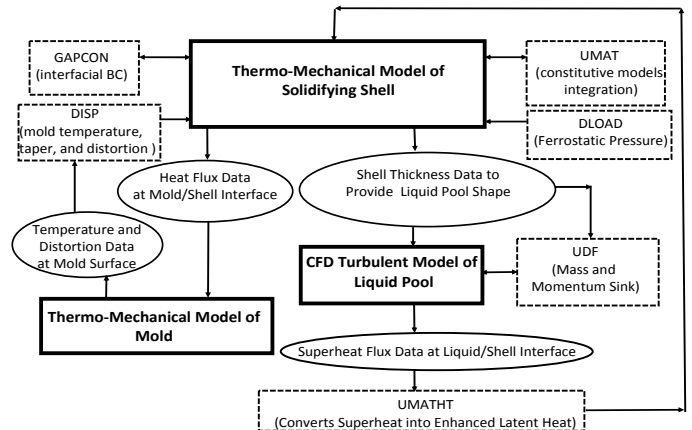


Figure 7: Flow Chart for Multiphysics Solution Strategy

The flange pushes on the shell, creating good contact and suggesting flange taper is excessive, as shown in **Figure 8 a**). Small gaps form, but divergent 2-D heat transfer from the corner produces a thick, cold shell in this region. This contact pressure from the middle of the flange causes outward buckling and bending of the shell in the shoulder region. Furthermore, the shoulder region of the beam-blank mold has a convex shape which converges heat flow and increases local temperature, opposite to behavior at the corners. Heat extraction from the shoulder is therefore retarded as shown in **Figure 8 b**), producing a thinner shell with higher temperature. This causes stress concentration in the shoulder area, where the maximum tensile stress and strains are observed. Longitudinal cracks and breakouts are often found in this same shoulder region. The

breakout shell obtained from the commercial caster pictured in **Figure 9 a)** was initiated at the thin shoulder region [26].

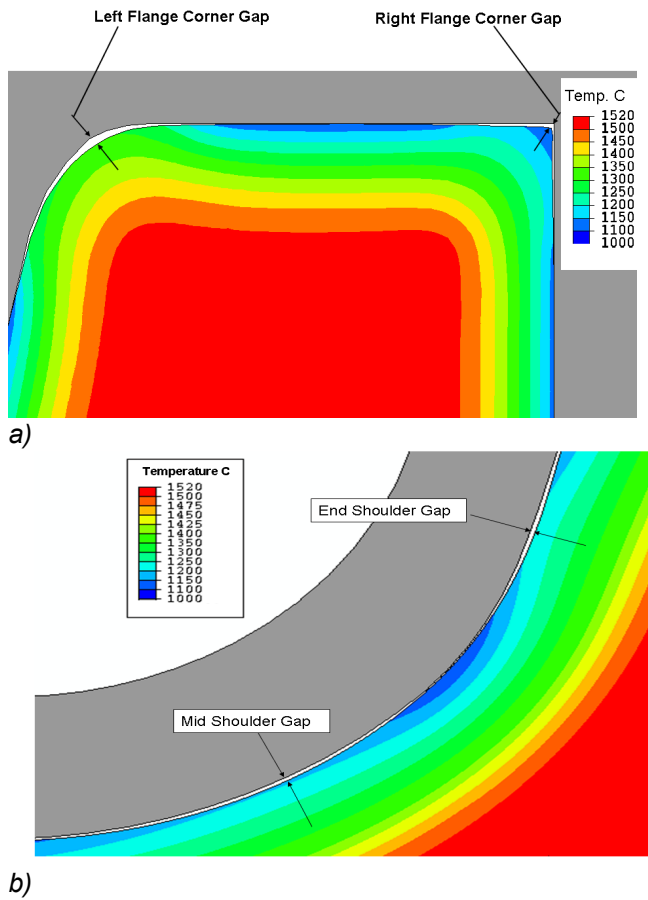


Figure 8: Beam-Blank Shell Temperature Contours and Gaps in a) Flange Region; b) Shoulder Region

Finally, the shell thickness at 90% liquid predicted by both models is compared with measurements around the perimeter of the breakout shell in Figure 9 c). The labels for the positions around the perimeter are explained in Figure 9 b). The initial thermo-mechanical model assuming a uniform superheat distribution can only roughly match the shell thickness variations. Shell thickness variations at the corners and shoulder due to air gap formations were captured owing to the interfacial heat transfer model. However, the middle portion of the wide face is 4 mm thicker in the measurement. This is evidently caused by the uneven superheat distribution due to the flow pattern in the liquid pool, as this location is farthest away from the pouring funnels and has the least amount of superheat as shown in Figure 5. In contrast, the shoulder region receives the highest amount of superheat, so the measured shell thickness there is more than 2 mm thinner than the initial thermo-mechanical model prediction. Further modelling produced improved taper designs, which involved decreasing taper in the flange region (to

lessen flange pushing), and increasing taper in the shoulder region (to lessen gap formation).

The improved multiphysics model that includes the fluid flow effects matches the shell thickness measurement around the entire perimeter much more accurately. This finding illustrates the improved accuracy that is possible by including the effects of fluid flow into a thermal stress analysis of solidifying shells.

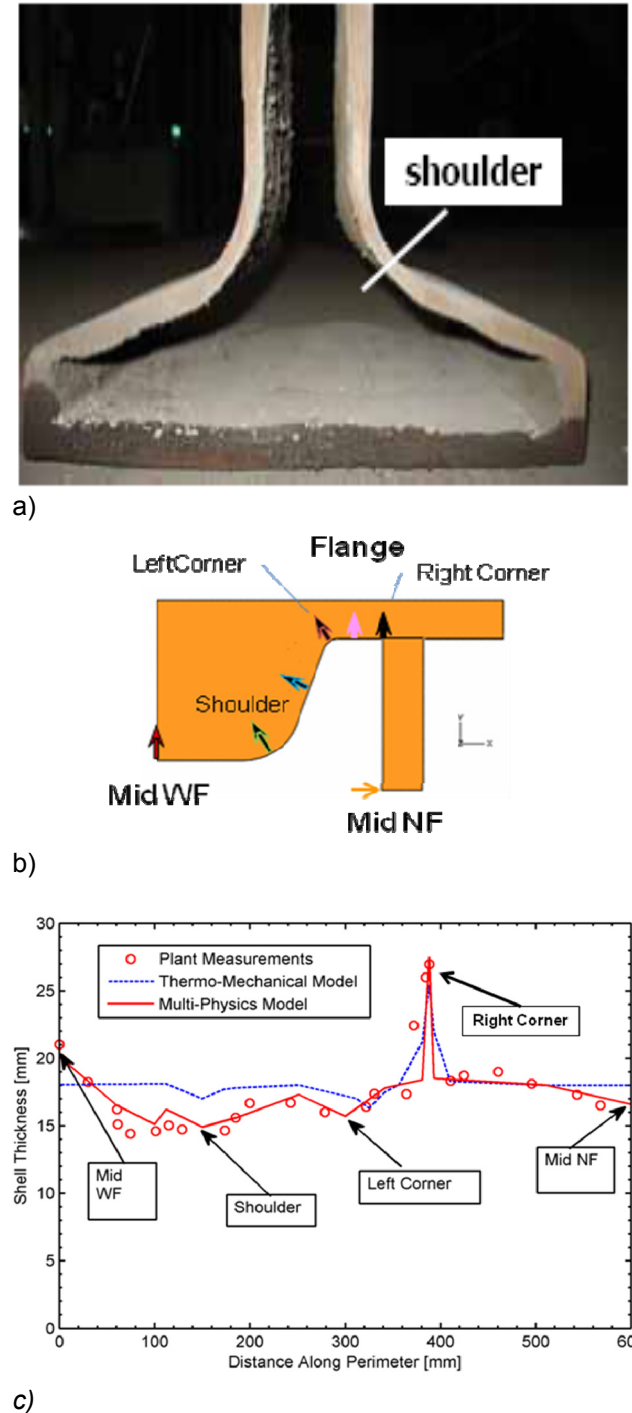


Figure 9: Solidified Steel Shell Thickness a) Breakout Shell; b) location Labels; c) Comparisons

Conclusions

This paper illustrates an effective approach for accurate multiphysics modeling of commercial solidification processes. The complex multiphysics phenomena of continuous casting are uncoupled into separate simulations of the molten fluid flow region, the mushy zone and solid steel shell region, and the mold. Super-heat fluxes, delivered by turbulent fluid flow to the solidification front, are calculated with a finite-volume fluid flow model in FLUENT. A new latent-heat method incorporates these results into a coupled thermo-mechanical model of the solidifying shell using a finite-element model in ABAQUS. A complete finite-element thermal-stress analysis of mold thermal distortion is incorporated through a second database and boundary condition at the shell-mold interface. The model is demonstrated by simulating solidification in a one-quarter transverse section of a commercial beam blank caster with complex geometry, temperature dependent material properties, and realistic operating conditions. The results compare well with in-plant measurements of the thickness of the solidifying shell from a breakout.

Acknowledgements

We would like to thank Clayton Spangler and the Steel Dynamics Structural and Rail Mill in Columbia City, Indiana for their great support of this project, and the National Center for Supercomputing Applications (NCSA) for computational and software resources. Funding of this work by the Continuous Casting Consortium at the University of Illinois and the National Science Foundation Grant # CMMI 07-27620 is gratefully acknowledged.

References

- [1] C. Bailey, S. Bounds, M. Cross, G. Moran, K. Pericleous, G. Taylor, Multiphysics modeling and its application to the casting process, *Comp. Modeling and Sim. in Eng.*, vol. 4(3), pp. 206-212, 1999.
- [2] O. Ludwig, M. Aloe, P. Thevoz, S. Scott, A. Sholapurwalla, State of the art in modeling of continuous casting, *Proc. AISTech 2009 Iron and Steel Technology*, vol. 2, pp. 883-891, 2009.
- [3] J. Lee, T. Yeo, Kyu H. OH, J. Yoon, and U. Yoon, Prediction of Cracks in Continuously Cast Steel Beam Blank through Fully Coupled Analysis of Fluid Flow, Heat Transfer, and Deformation Behavior of a Solidifying Shell, *Metal. and Materials Transactions A*, vol. 31A, pp. 225-237, 2000.
- [4] A. Teskeredzic, I. Demirdzic, S. Muzaferija, Numerical method for heat transfer, fluid flow, and stress analysis in phase-change problems, *Numerical Heat Transfer B*, vol. 42(5), pp. 437-459, 2002.
- [5] A. Chatterjee, V. Prasad, A Full 3-Dimensional Adaptive Finite Volume Scheme for Transport and Phase-change Processes, Part I: Formulation and Validation, *Numerical Heat Transfer A*, vol. 37(8), pp. 801-821, 2000.
- [6] C. Del Borello, E. Lacoste, Numerical Simulation of the liquid flow into a porous medium with phase change change: Application to Metal Composites Processing, *Numerical Heat Transfer A*, vol. 44(7), pp. 723-741, 2003.
- [7] M. R. Shamsi, S. K. Ajmani, Three Dimensional Turbulent Fluid Flow and Heat Transfer Mathematical Model for the Analysis of a Continuous Slab Caster, *ISIJ International*, vol 47(3), pp. 433-442, 2008.
- [8] M. Pokorny, C. Monroe, C. Beckermann, L. Bichler, C. Ravindran, Prediction of Hot Tear Formation in Magnesium Alloy Permanent Mold Casting, *Int. J. Metalcasting*, vol, 2(4), pp. 41-53, 2008.
- [9] A.N.O. Moraga, D. C. Ramirez, M.J. Godoy, P. D. Ticchione, Study of convection non-newtonian alloy solidification in moulds by the PSIMPLER/finite-volume method, *Numerical Heat Transfer A*, vol. 57(12), pp. 936-953, 2010.
- [10] R. Pardeshi, A. K. Singh, P. Dutta, Modeling of solidification processes in a rotary electromagnetic stirrer, *Numerical Heat Transfer A*, vol. 55(1), pp. 42-57, 2009.
- [11] D. Sun, S. V. Garimella, Numerical and experimental investigation of solidification shrinkage, *Numerical Heat Transfer A*, vol. 52(2), pp. 145-162, 2007.
- [12] S. Koric and B. G. Thomas, Efficient Thermo-Mechanical Model for Solidification Processes. *International Journal for Num. Methods in Eng.*, vol 66, pp. 1955-1989, 2006.
- [13] Koric, S., L.C. Hibbeler, R. Liu, and B.G. Thomas, "Multiphysics Model of Metal Solidification on the Continuum Level," *Numerical Heat Transfer, Part B: Fundamentals*, vol. 58(6), pp. 371-392, 2010.
- [14] S. Koric, B. G. Thomas, V. R. Voller, Enhanced Latent Heat Method to Incorporate Superheat Effects into Fixed-grid Multiphysics Simulations, *Numerical Heat Transfer Part B*, vol. 57, pp. 396-413, 2010.
- [15] ABAQUS User Manuals v. 6.9, Dassault Systems Simulia Corp., 2009.
- [16] A. Grill, J. K. Brimacombe, F. Weinberg, Mathematical analysis of stress in continuous casting of steel. *Ironmaking Steelmaking*, vol. 3, pp. 38-47, 1976.

- [17] F. G. Rammerstrofer, C. Jaquemar, D.F Fischer, H. Wiesinger, Temperature fields, solidification progress and stress development in the strand during a continuous casting process of steel, *Numerical Methods in Thermal Problems*, Pineridge Press, pp. 712-722, 1979.
- [18] J. O. Kristiansson, Thermomechanical behavior of the solidifying shell within continuous casting billet molds- a numerical approach, *Journal of Thermal Stresses*, vol. 7, pp. 209-226, 1984.
- [19] D. Celentano, S. Oller, E. Onate, A coupled thermomechanical model for the solidification of cast metals. *Int. J. of Solids and Structures*, vol. 33(5), pp. 647-673, 1996.
- [20] H. Zhu, Coupled thermal-mechanical finite-element model with application to initial solidification, Ph.D Thesis University of Illinois, 1993.
- [21] C. Li, B. G Thomas, Thermo-Mechanical Finite-Element Model of Shell Behavior in Continuous Casting of Steel, *Metal. & Material Trans. B.*, vol. 35B(6), pp. 1151-172, 2004.
- [22] J. M. Risso, A. E. Huespe, A. Cardona, Thermal stress evaluation in the steel continuous casting process, *International Journal of Numerical Methods in Engineering*, vol. 65(9), pp. 1355-1377, 2005.
- [23] S. Koric, L. C. Hibbeler, B. G. Thomas, Explicit coupled thermo-mechanical finite element model of steel solidification, *International Journal for Numerical Methods in Engineering*, vol. 78, pp. 1-31, 2009.
- [24] J. K. Park, B. G. Thomas BG, I. V Samarasekera, Analysis of Thermo-Mechanical Behavior in Billet Casting with Different Mold Corner Radii, *Ironmaking and Steelmaking*, vol. 29(5), pp. 359-375, 2002.
- [25] H. N Han, J. E Lee, T. J Yeo, Y. M. Won, K. Kim K, K. H. Oh, J. K Yoon, A Finite Element Model for 2-Dimensional Slice of Cast Strand, *ISIJ International*, vol. 39(5), pp. 445-455, 1999.
- [26] L. C. Hibbeler, S. Koric, K. Xu, C. Spangler, B. G. Thomas, Thermomechanical Modeling of Beam Blank Casting, *Iron and Steel Technology*, vol. 6(7), pp. 60-73, 2009.
- [27] Y. M. Won, B. G. Thomas, Simple Model of Microsegregation During Solidification of Steels, *Metal. and Material Trans. A*, vol. 32A(7), pp. 1755-1767, 2001.
- [28] P. F. Kozlowski, B. G. Thomas, J. A. Azzi, H.Wang, Simple constitutive equations for steel at high temperature, *Metal. and Material Trans. A*, vol. 23A, pp. 903-918, 1992.
- [29] R. D. Cook, D. S. Malkus, M. E. Plesha, R. J. Witt, *Concepts and Applications of Finite Element Analysis*, 4th ed., pp. 1-784, John Wiley & Sons, Inc., Hoboken, NJ, 2001.
- [30] J. A. Dantzig, C. L. Tucker III, *Modeling in Materials Processing*, 1st ed., pp. 282-321, Cambridge University Press, Cambridge, UK, 2001.
- [31] B. E Launder, D. B. Spalding, *The Numerical Computation of Turbulent Flows*, *Comput. Methods Appl. Mech. Eng.*, vol. 3, pp. 269-289, 1974.
- [32] *Fluent User Manuals v6.3*, Ansys Inc., 2008.
- [33] H. K. Versteeg, W. Malalasekera, *An Introduction to Computational Fluid Dynamics*, Second Ed., New York, NY:Pearson Prentice Hall, 2008.
- [34] B. Rietow, *Fluid Velocity Simulations and Measurements in Thin Slab Casting*, MS Thesis, University of Illinois, 2007.
- [35] S. Mahmood, *Modeling of Flow Asymmetries and Particle Entrapment in Nozzle and Mold During Continuous Casting of Steel Slabs*, MS Thesis, University of Illinois, 2006.
- [36] J. K Park, B. G Thomas, I. V Samarasekera, U. S. Yoon, *Thermal and Mechanical Behavior of Copper Moulds During Thin Slab Casting (i): Plant Trail and Mathematical Modeling*, *Metall. Mater. Trans. B*, vol. 33B, pp. 425-436, 2002.
- [37] J. H. Weiner, B. A. Boley, *Elasto-plastic thermal stresses in a solidifying body*, *J. Mech. Phys. Solids*, vol. 11, pp. 145-154, 1963.